Structural evolution and the role of native defects in subnanometer MoS nanowires

Daniel F. Souza,[1,2] Andréia L. Rosa ●,[1] Pedro Venezuela,[3] José E. Padilha ●,[4] Adalberto Fazzio,[5] and Renato B. Pontes ●[1,*]

[1]*Instituto de Física, Universidade Federal de Goiás, Campus Samambaia, 74690-900 Goiânia, Goiás, Brazil*
[2]*Instituto Federal do Amazonas, 69020-120 Manaus, Amazonas, Brazil*
[3]*Instituto de Física, Universidade Federal Fluminense, 24210-346 Niterói, Rio de Janeiro, Brazil*
[4]*Universidade Federal do Paraná, Campus Avançado de Jandaia do Sul, Jandaia do Sul, Paraná, Brazil*
[5]*Brazilian Nanotechnology National Laboratory (LNNano)/CNPEM, PO Box 6192, 13083-970 Campinas, São Paulo, Brazil*

We carried out first-principles calculations based on density functional theory aiming to understand the structural evolution along the stretching process and the impact of native defects in metallic subnanometer MoS nanowires (NWs). By pulling the pristine NWs quasistatically, we investigate the full structural evolution along the stretching process until the nanowire breaking point, obtaining a maximum applied stress (force) of ≈ 18.9 GPa (7.1 nN). On the other hand, since the existence of intrinsic defects is likely to occur in these samples, we show that under S-rich conditions a sulfur antisite is found to be the energetically most stable defect, and under Mo-rich conditions a sulfur vacancy has the lowest formation energy. Our results also reveal that these defects present local reconstruction that can be clearly identified by the simulated scanning tunneling microscopy images. Furthermore, through a detailed analysis of the electronic structure, we verify that with the exception of the Mo interstitial and S antisite, all defects preserve the metallic behavior of the MoS nanowires.

I. INTRODUCTION

Nanoelectronics aims at the development of nanoscaled devices operating in the quantum regime in order to face the dramatic challenges at the end of the road map for highly scaled complementary metal-oxide semiconductor (CMOS) devices [1–3]. A difficult task in the pursuit of ultrasmall electronic components is the obtention of novel materials with reduced dimensions [4,5].

However, with the isolation of graphene, a new era in the field of materials science has started [6,7]. Thus, the interest of the scientific community in graphene [8–11] and other low-dimensional materials, such as hexagonal boron nitride (h-BN) [12,13], silicene (h-Si) [14–16], germanene (h-Ge) [17,18], black and blue phosphorene [19–22], transition-metal oxides (TMOs) [23–25], and transition-metal dichalcogenides (TMDCs) [26–28], has increased since these materials can exhibit novel physical and chemical properties [29–31] that will open new routes for different applications in nanotechnology.

In particular, TMDCs present a unique combination of atomic-scale thickness, interesting transport and mechanochemistry properties, the existence of an electronic band gap, and strong spin-orbit coupling, which make them interesting for fundamental studies and for applications in high-end electronics, spintronics, optoelectronics, energy-harvesting, flexible electronics, and biomedical applications [32–37].

On the other hand, metallic nanowires [38–44] are another class of materials which have attracted strong interest for

applications, ranging from transistor electronics to interconnects, due to their versatile properties such as high electrical and thermal conductivity, optical transparency, chemical inertness, quantum conductance, and the capacity to produce atomic chains [41,45–47], which are quite challenging to obtain since they are often unstable and fragile.

Nevertheless, recent investigations have revealed that metallic subnanometer wires interconnecting domains of monolayer transition-metal dichalcogenides can be controllably fabricated by using the electron beam from a scanning transmission electron microscope (STEM) [48–50]. Similar experimental realizations were already successfully performed to determine the structure and the quantized conductance behavior of coinage metals such as copper (Cu) [51], silver (Ag) [52], and gold (Au) [53]. This technique was also employed for deriving carbon atomic chains from graphene [54].

Essentially, the experiments are carried out at room temperature and the possible local heating caused by the collision of the electron is thermalized in a matter of picofemtoseconds considering the single-layer TMDC thermal conductivity and the dimensions of the nanoconstriction. The energy of the incident electrons is between 60–80 kV, which might either cause the creation of a hole by the extraction of Mo (or W) and S (or Se) atoms or the formation of defects, in a specific region of the monolayer. Repeating the process in an adjacent region creates a nanoribbon confined by the two holes. The nanoribbon reconstructs and shrinks to form the wire via atomic diffusion. By the processes described above, the structure changes its stoichiometry from MoS_2 to MoS [48].

Intrinsic defects may be present at all stages of the subnanometer nanowire formation [50,55]. It is verified that both

*pontes@ufg.br

natural sources or laboratory-grown transition-metal dichalcogenides have defects such as antisites, vacancies, divacancies, line defects, and even impurities [56–60]. The intrinsic defects can also be created when the TMDC monolayer is under intense electron beam irradiation [61,62]. Since the introduction of well-controlled defects plays a crucial role in the physical properties of nanostructured materials, and therefore a potential route for tuning new functionalities, it is very important to investigate how defects can affect the structural and electronic properties of the TMDC nanowires.

Motivated by these recent experiments, in this work, by performing state-of-the-art solid-state simulations, we investigate the structural and electronic properties of pristine and defective MoS nanowires. We show that the pristine nanowires are mechanically stable, presenting a metallic character. Our results also reveal that vacancies, antisites, adatoms, and interstitial defects present a local reconstruction that can be clearly identified by scanning tunneling microscopy (STM) images. In addition, we verify that the molybdenum antisite has the lowest formation energy at S-rich conditions, while the sulfur interstitial is more stable at Mo-rich conditions. From the electronic point of view, the Mo-interstitial and S-antisite defects create narrow band gaps in the nanowire, whereas the others defects preserve the metallic feature of the MoS nanowire.

II. COMPUTATIONAL DETAILS

All calculations of the atomic structure and electronic properties of the MoS nanowires were performed within the density-functional-theory (DFT) framework [63–65] as implemented in the open-source package for material explorer (OPENMX) [66,67]. For the exchange-correlation functional, we use the generalized gradient approximation (GGA) in the scheme of Perdew-Burke-Ernzerhof (PBE) [68]. The core Coulomb potential is treated by a norm-conserving pseudopotential proposed by Morrison *et al.* [69], which is a norm-conserving version of the ultrasoft pseudopotential by Vanderbilt [70]. A basis set consisting of a linear combination of the localized pseudoatomic orbitals and an energy cutoff of 300 Ry were used to expand the Kohn-Sham orbitals and to represent the charge density on the grid [66,71]. The spin-orbit interaction was included via a norm-conserving, fully relativistic, j-dependent pseudopotentials scheme, in the noncollinear spin-DFT formalism [72]. The Brillouin zone was sampled according to the Monkhorst-Pack scheme [73] with a grid of $1 \times 1 \times 10$ $\vec{k}$ points. We used periodic boundary conditions with a supercell of 60 atoms (5 unit cells) for the isolated pristine MoS nanowires. To avoid the interaction between the neighboring wires, a vacuum space between them was set larger than 15 Å in the directions perpendicular to the wire axis. The structural relaxation was performed until the forces acting on each atom were less than 0.01 eV/Å. To investigate the rupture process, the supercell was increased in steps of 0.2 Å and, for each new length, the system was fully relaxed. This procedure was followed until the rupture. The force was calculated as $F = (\partial E_{tot}/\partial \Delta L)$, where E_{tot} is the total energy of the system at each stretching and ΔL stands for the elongation of the system. The STM images (using the WSXM software package [74]) were simulated by
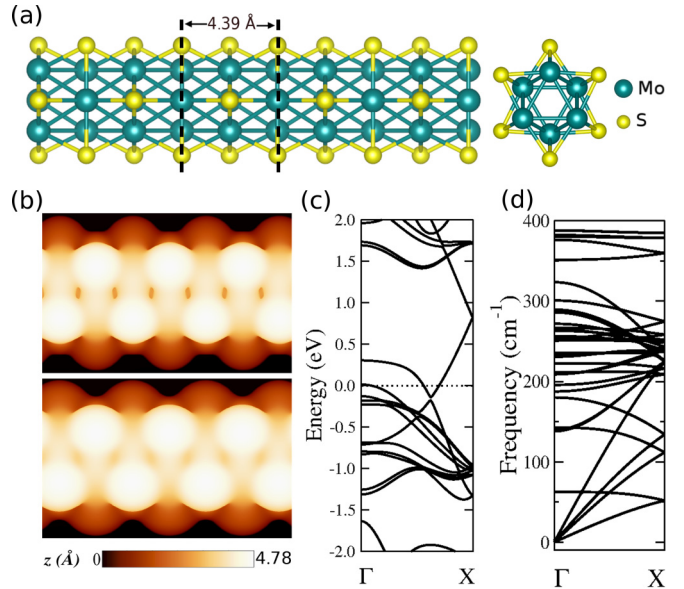

FIG. 1. (a) Ball-and-stick representations (top and front views) of the optimized geometric structure of a pristine MoS nanowire. The dashed black lines indicate the unit cell. (b) STM-simulated images of the MoS nanowire. The STM images were simulated by using a voltage between the tip and the sample of $E_F + 0.5$ eV (upper panel) and $E_F - 0.5$ eV (lower panel). The scale bar in the STM images is given in Å. (c) Electronic band structure and density of states. The Fermi energy is set to zero. (d) Low frequencies of the phonon spectrum for the pristine MoS nanowire.

using the procedure proposed by Tersoff-Hamann [75]. The stability of the system was determined by calculating the phonon dispersion with the PHONOPY code [76].

III. RESULTS AND DISCUSSION

A. Structure

The unit cell of an isolated MoS nanowire consists of two staggered triangles composed of MoS units. In Fig. 1(a), we show the top and front views the atomic structure of the nanowires, which are taken from STEM images from Ref. [48]. In these experimental images, it is possible to determine the atomic positions of the wires. The calculated equilibrium lattice parameter along the axis wire was 4.39 Å, in good agreement with previous theoretical and experimental results [48,77,78]. We also obtained Mo-S (Mo-Mo) bond lengths of 2.52 Å (2.79 Å), if they lie in the same plane, and 2.55 Å (2.72 Å), if the atoms are in adjacent planes. These interatomic distances are in very good agreement with the values of 2.49 Å (2.74 Å), for in-plane distances, and 2.62 Å (2.69 Å), for the distances between the planes, obtained by Vilfan [77]. In Fig. 1(b), we show DFT-simulated STM images for the empty [Fig. 1(b), upper panel] and occupied [Fig. 1(b), lower panel] states within $E_F \pm 0.5$ eV for a pristine MoS nanowire. The brighter regions are associated to the sulfur atoms. There is no pronounced difference between the images. However, it is worthwhile to mention that the brighter regions in Fig. 1(b) (lower panel) are a little wider as a consequence of the higher density of states in that region of energy.
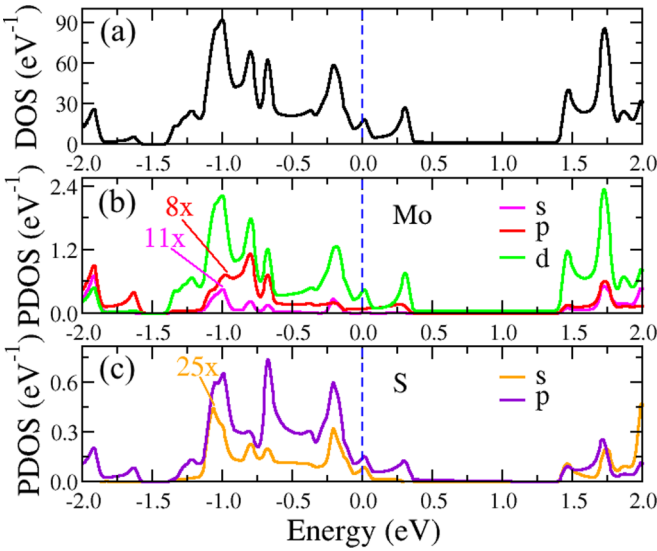
FIG. 2. Pristine MoS nanowire: (a) DFT-calculated total density of states (DOS). (b),(c) Projected density of states (PDOS) of S and Mo, respectively. The Fermi level is set to zero.

Our DFT results for the electronic structure of the pristine MoS nanowire are presented in Fig. 1(c). The results show that the subnanometer pristine MoS nanowire is indeed a metal. To investigate the mechanical stability of the pristine one-dimensional (1D) nanowire, we calculated its phonon dispersion. We have considered, in this work, the finite-displacement approach with supercell sizes of $1 \times 1 \times 4$ primitive unit cells. The result is presented in Fig. 1(d). We do not verify the presence of imaginary frequencies in the Brillouin zone. In this way, our results indicate that this system is mechanically stable. In addition, four acoustic modes are clearly visible. The two linear modes correspond to the longitudinal and torsional modes. The other two modes correspond to flexural modes, which are characteristic for quasi-one-dimensional systems. This result is in agreement with previous works [79,80].

In Figs. 2(a)–2(c), we present the total density of states (DOS) and partial density of states (PDOS) for the optimized structure of the pristine MoS nanowire presented in Fig. 1(a). From the projected density of states shown in Figs. 2(b) and 2(c), we can see that the region in the vicinity of the Fermi energy is mainly contributed by the $4d$ orbitals of Mo atoms. In particular, the Mo d_{xy}, $d_{x^2-y^2}$, and d_{z^2} orbitals play a crucial role in the determination of the metallic characteristics of this nanowire (see the Supplemental Material [81]).

As the nanowire can be created from the MoS_2 sheet, to understand the origin of the metallic behavior, we start the discussion from monolayer MoS_2. The 2D MoS2 presents a hexagonal lattice with a single Mo atom intercalated between two S atoms and it exhibits a direct band gap of 2.06 eV (at the K point) [82,83]. The valence band at the K point is composed of S p_x and p_y orbitals, and Mo d_{xy} and $d_{x^2-y^2}$ orbitals, which are oriented along the in-plane direction. The conduction band, at the K point, is mainly contributed by S p_x and p_y orbitals and Mo d_{z^2} orbitals [82]. As a consequence of the structural confinement, the stoichiometry of the system

changes since now the formula unit is MoS. The nanowire now exhibits metallic Mo-Mo bonds [see Fig. 1(a)]. Such bonds do not appear in monolayer MoS_2. The effect in the electronic structure is that the Mo d_{z^2} orbital is shifted to the Fermi energy. Also, in the vicinity of the Fermi energy, a strong hybridization between the Mo d_{xy} and $d_{x^2-y^2}$ orbitals occurs. Furthermore, there is an additional hybridization between the d orbitals of the Mo atoms with the p_x and p_y orbitals of the S atoms (see Supplemental Material [81]). All of these contributions together explain the metallic characteristics of this subnanometer nanowire.

B. Structural evolution

One important point about those 1D structures is the dynamics of rupture of the systems. It provides valuable information about the stiffness of the system and others mechanical properties. Moreover, as the MoS nanowires may be used as interconnects in future flexible nanocircuits and since the variation of the transport properties is strongly correlated with structural changes of the material, it is an important first step to understand the stretching process (until the rupture). Thus, the full structural evolution of a pristine MoS nanowire until the breaking point is investigated. Nine representative geometries and 2D contour plots of the electronic charge density, as a function of the strain, are shown in Fig. 3 (upper panels). As the nanowire is pulled, for small strains [Fig. 3, ball-and-stick models (1)–(3)], the Mo-S and Mo-Mo bond lengths increase. However, no significant reconstructions, lattice distortions, or even chemical bond breaking is observed (the first elastic stage). By increasing the strain [ball-and-stick models (4) and (5)], it is possible to verify some reconstructions in the central region of the nanowire. For slightly higher strains [Fig. 3, ball-and-stick models (6) and (7)], lattice distortions are present. Moreover, it is possible to see additional reconstructions and other Mo-Mo and Mo-S bond breaking now, distributed along the nanowire. The final elastic stage is characterized by the increasing of the Mo-S and Mo-Mo bond lengths [Fig. 3, ball-and-stick model (8)]. Lastly, the rupture of the nanowire occurs [Fig. 3, ball-and-stick model (9)].

In Fig. 3 (lower panels), we also present the total energy and stress (σ) as a function of the strain (ε). The strain (in percentage) was calculated as $\varepsilon = \frac{l-l_0}{l_0}$, where l_0 is the equilibrium supercell length along the nanowire growth direction. Stress was calculated from the energy-strain curve as

$$\sigma = \frac{1}{V} \frac{dE}{d\varepsilon},$$

where σ is the longitudinal stress, V is the volume of the MoS nanowire, ε is the strain, and E is the strain energy of the nanowire. We consider the volume of an isolated nanowire as $V = Al = \pi r^2 l$, where r is the radius of the wire and l is the length of the nanowire supercell. Due to the difficulty in defining the cross-sectional area, we assume the area of the wire as the area of a circle whose radius is equal to the distance of the S atoms to the axis of the wire ($A = 0.27$ nm^2). Thus, a value for Young's modulus, defined as the slope of the stress-strain curve in the first elastic deformation region, of approximately 740 GPa is achieved. A comparable value
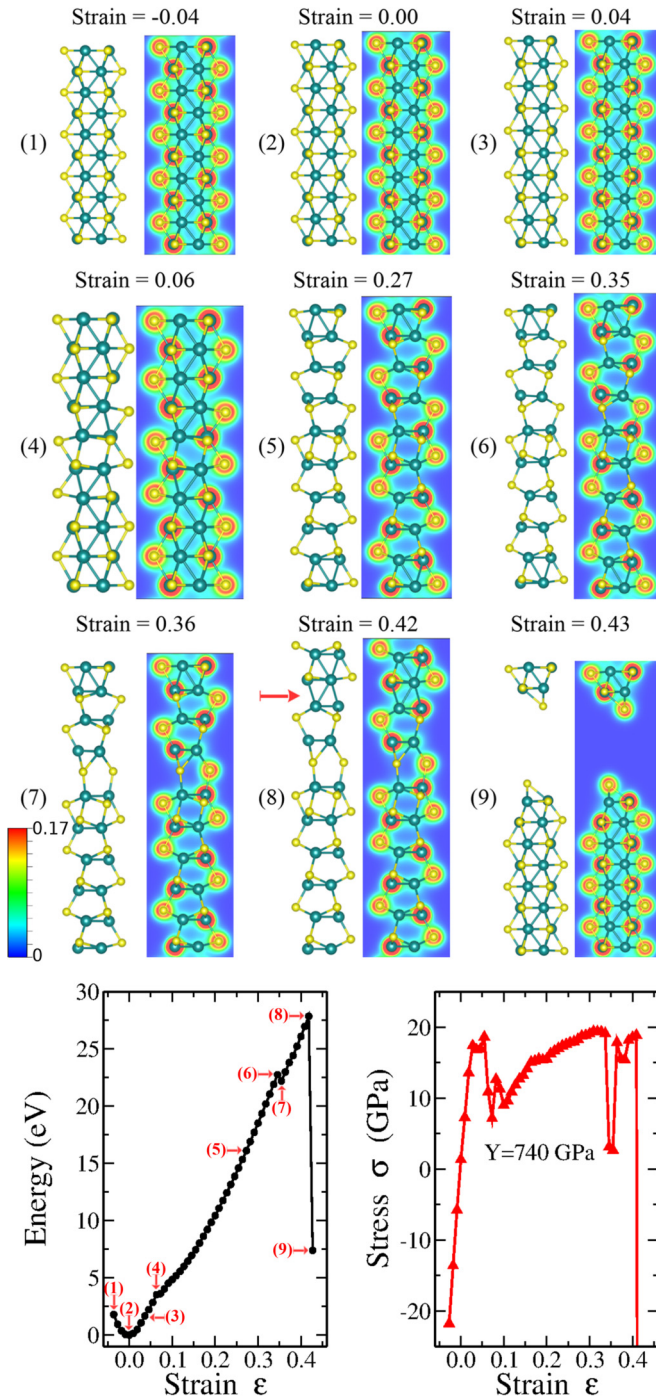
FIG. 3. Upper panels: (1–9) Ball-and-stick representations and 2D contour plots of the electronic charge density of the different stages along the stretching process of a pristine MoS nanowire. The red arrow, in panel 8, indicates the rupture point. Lower panels: Total energy (eV) and stress (GPa) as a function of the strain. The total-energy values are displayed relative to the lowest-energy structure (shown in panel 2). The inset in the stress-strain plot is the computed value for the Young's modulus.
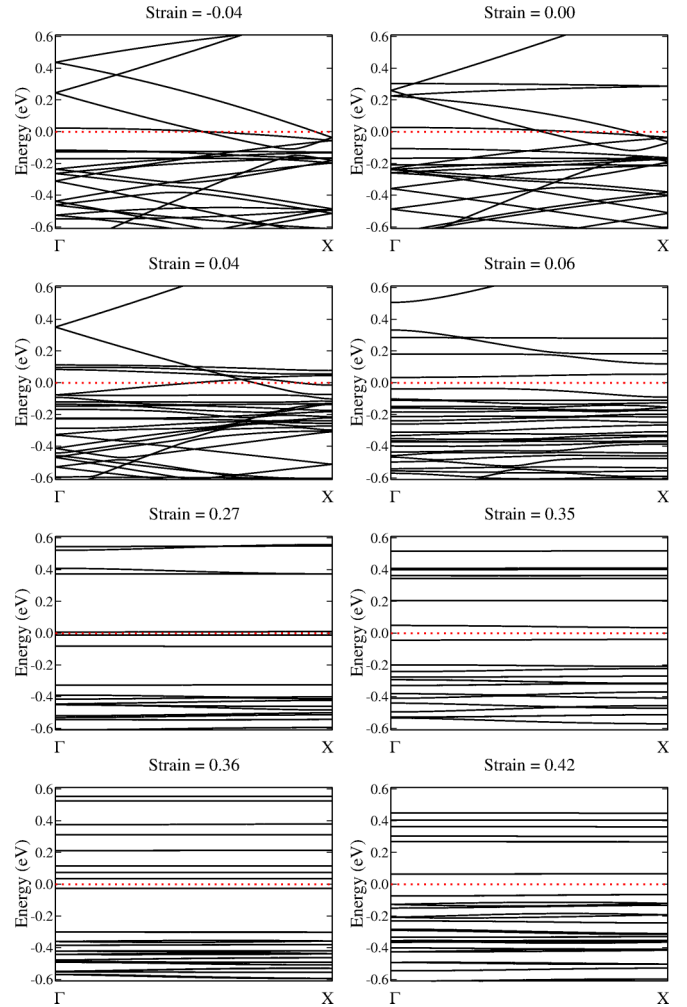

FIG. 4. DFT-PBE electronic band structure as a function of the strain for the pristine MoS nanowire. The dotted lines indicate the Fermi energies.

stress was roughly 18.9 GPa at a strain of ≈ 0.4. In addition, we calculate a value for the applied force just before the rupture of ≈ 7.1 nN (see the Supplemental Material [81]).

In Fig. 4, we show the band structures as a function of strain. The first point to note is that when slightly compressed (strain -3.64%), the isolated MoS nanowire preserves its metallic character. Under stretching, the metallic behavior is kept until $\approx 5\%$ of strain. After that, as can be seen in Fig. 3, ball-and-stick models (4)–(9), the Mo-Mo and Mo-S bonds start to break and bond reconstructions in the atomic structure are verified, which leads the nanowire to exhibit a small-gap semiconductor character. Also, as a function of the stretching, more and more atomic bonds are broken and, consequently, it is possible to see localized flat-band states.

C. Defect formation energies, STM fingerprints, and electronic band structures

In order to verify the thermodynamic stability of the investigated defect complexes, we follow the approach derived by van de Walle and Neugebauer [86]. The formation energy of

(705 GPa) was obtained by performing DFT plane-wave calculations using the VASP code [84,85] (see the Supplemental Material [81]). The existence of negative stresses means that the system is under compression. The calculated breaking
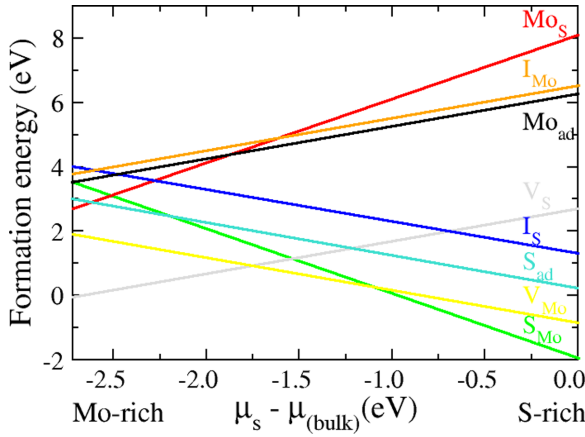
FIG. 5. Calculated formation energies (in eV) for native defects in MoS nanowires at the neutral charge state in Mo- and S-rich growth conditions.

a neutral defect in a wire is thus defined as

$$E_f = E_{\text{tot}}^{\text{defect}} - E_{\text{tot}}^{\text{perfect}} - \sum_i n_i \mu_i,$$

where $E_{\text{tot}}^{\text{defect}}$ is the total energy of a defective wire, $E_{\text{tot}}^{\text{perfect}}$ is the total energy of a perfect MoS wire, n_i is the number of defect atoms of type i that have been added to or removed from the wire, and μ_i is the corresponding chemical potential of each species. The lower bound of the chemical potential corresponds to the total absence of impurities/defects in the material. An upper bound on the chemical potential is given by the energy of the elemental bulk phase or other solubility-limiting phases. The formation of metallic Mo can be avoided by imposing its chemical potential to obey to $\mu_{\text{Mo}} \leqslant \mu_{\text{Mo(Mo−bulk)}}$, where Mo bulk is the total energy of molybdenum bulk in a bcc structure. Similarly, the sulfur chemical potential is set to obey $\mu_S \leqslant \mu_{S(S−bulk)}$. We chose $\mu_{S−bulk}$ as the total energy of the solid α structure. The accessible range of chemical potentials is governed by the MoS$_2$ formation enthalpy $\Delta H^{\text{MoS}_2} = \mu_{\text{MoS}_2} - \mu_{\text{Mo(Mo−bulk)}} - \mu_{\text{S(S−bulk)}}$. However, the sulfur and molybdenum chemical potentials are not independent, but related by $\mu_{\text{MoS}_2} = \mu_{\text{Mo}} + 2\mu_S$. By combining the former two equations, we obtain the limits for the sulfur chemical potential $\Delta H^{\text{MoS}_2} \leqslant \mu_S - \mu_{S−bulk} \leqslant 0$. We neglect the temperature dependence on the sulfur chemical potential. The formation enthalpy of the molybdenum disulfide sheet is calculated to be $\Delta H^{\text{MoS}_2} = -2.72$ eV compared with the experimental value of -2.44 eV at room temperature [87]. The formation enthalpy of a pure MoS nanowire is found to be -1.00 eV, meaning that such a nanostructure is thermodynamically stable.

The calculated formation energy for the considered intrinsic defects in MoS nanowires is presented in Fig. 5. There are three defects which are stable in the wire. Under S-rich conditions, a sulfur antisite is found to be stable. Under Mo-rich conditions, a sulfur vacancy has the lowest formation energy. An additional structure containing a molybdenum vacancy is stable at intermediate values of the sulfur chemical potential.
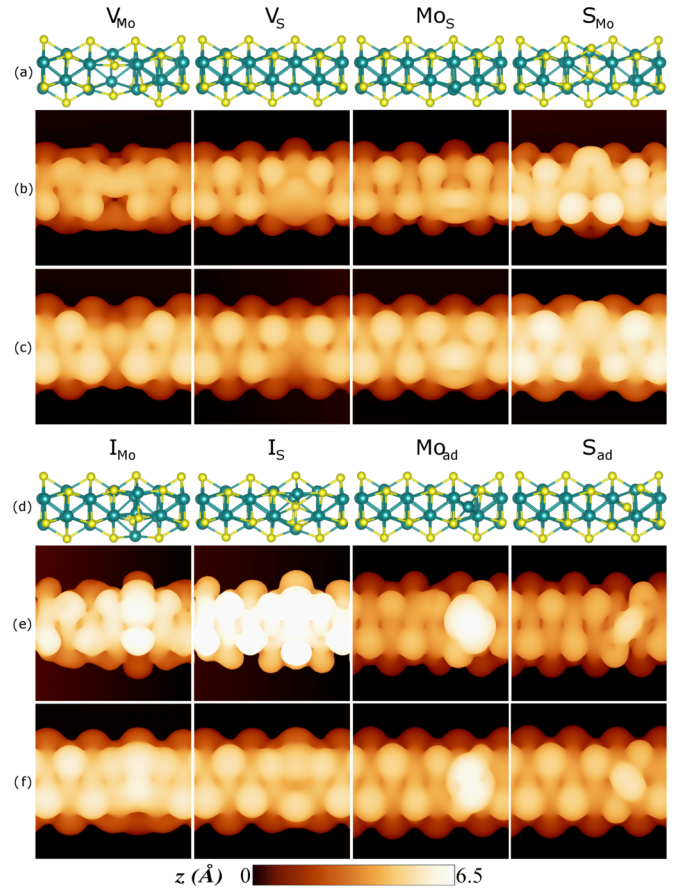

FIG. 6. (a),(d) Ball-and-stick representations of the optimized structures of the defective MoS nanowires. (b),(c),(e),(f) DFT-simulated STM images of the defective nanowires. The STM images were simulated by using a voltage between the tip and the sample of (b),(e) +0.5 eV and (c),(f) −0.5 eV. The scale bar is in Å.

Aiming to understand how the native defects modify the structural and the electronic properties of the MoS nanowires, in Fig. 6 we show the reconstructed structures and the DFT-simulated constant-height STM images of the defective nanowires. The Tersoff-Hamman approach was used to simulate STM images of both occupied and empty states, within $E_F \pm 0.5$ eV. On the STM images, the higher atoms are brighter than the lower atoms. The important point to note is that the presence of vacancies (V_{Mo}, V_S), antisites (Mo_S, S_{Mo}), or adatoms (Mo_{ad}, S_{ad}) leads to localized surface reconstruction, while interstices (I_{Mo}, I_S) induce extended reconstructions in this TMDC nanowire. In particular, the most stable defect under Mo-rich conditions (V_S) can be easily second column of Figs. 6(a), 6(b), and 6(c).

In Fig. 7, we present the DFT-calculated electronic band structure of the considered defects. We verify that all native defects considered, except the Mo interstitial (S antisite), preserve the intrinsic metallic character of the nanowire. The presence of a Mo interstitial (S antisite) modifies the structure of the nanowire. The obtained narrow band gap for this defect was ≈0.1 eV (≈0.06 eV). However, as shown in Fig. 5, this kind of defect has a high formation energy in both Mo-rich and S-rich conditions, indicating that it is
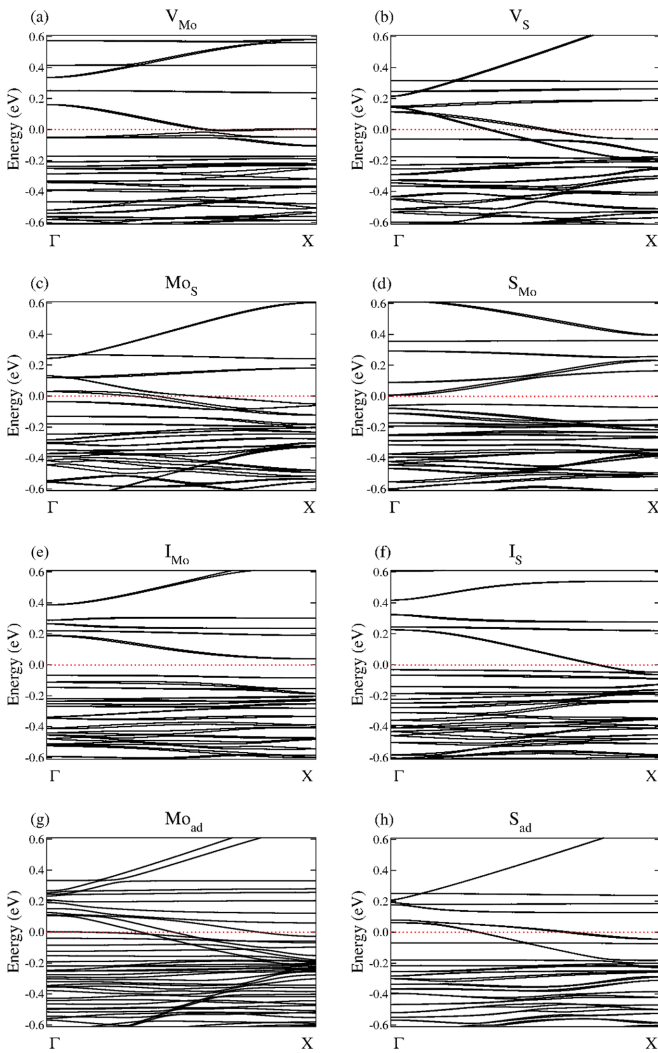
FIG. 7. DFT-calculated electronic band structure of the considered defects: (a) Mo vacancy, (b) S vacancy, (c) Mo antisite, (d) S antisite, (e) Mo interstitial, (f) S interstitial, (g) Mo adatom, and (h) S adatom. The Fermi energy is set to zero and indicated by the horizontal dotted line.

energetically unfavorable. Another interesting point to be noted is that the density of states in the vicinity of the Fermi energy is tunable, suggesting that under an appropriated defect engineering, the conducting properties of the nanowire can be tailored (see the Supplemental Material [81]). The maintenance of the metallicity for most of the native defects is an important result since this kind of nanowire has a huge potential to be used as interconnect elements in nanoelectronic devices.

IV. CONCLUSION

In conclusion, we used *ab initio* calculations based on density functional theory to investigate the structural evolution under the stretching process and the role of native defects in the electronic properties of metallic subnanometer MoS nanowires. By pulling the wire quasistatically, we obtain values for the applied force and stress right before the breaking of the nanowire around 7.1 nN and 18.9 GPa, respectively. In addition, we show that under S-rich conditions, a sulfur antisite is found to be the energetically most stable defect, and under Mo-rich conditions, a sulfur vacancy has the lowest formation energy. Moreover, we show that these defects present a local reconstruction that can be clearly identified by STM images and, with the exception of the Mo-interstitial and S-antisite, all defects preserve the metallic feature of the MoS nanowires. Our findings shed light on the electronic structure and its potential implications on the electrical properties of these 1D materials.

ACKNOWLEDGMENTS

[1] W. Lu and C. M. Lieber, Nat. Mater. **6**, 841 (2007).

[2] R. Chau, B. Doyle, S. Datta, J. Kavalieros, and K. Zhang, Nat. Mater. **6**, 810 (2007).

[3] A. Chen, J. Hutchby, V. Zhirnov, and G. Bourianoff, *Emerging Nanoelectronic Devices*, 1st ed. (Wiley, Hoboken, NJ, 2014).

[4] M. Zeng, Y. Xiao, Jinxin Liu, K. Yang, and L. Fu, Chem. Rev. **118**, 6236 (2018).

[5] F. F. Wang, X. Y. Hu, X. X. Niu, J. Y. Xie, S. S. Chuab, and Q. H. Gong, J. Mater. Chem. C **6**, 924 (2018).

[6] K. S. Novoselov, A. K. Geim, S. V. Morozov, D. Jiang, Y. Zhang, S. V. Dubonos, I. V. Grigorieva, and A. A. Firsov, Science **306**, 666 (2004).

[7] A. H. Castro Neto, F. Guinea, N. M. R. Peres, K. S. Novoselov, and A. K. Geim, Rev. Mod. Phys. **81**, 109 (2009).

[8] F. Bonaccorso, Z. Sun, T. Hasan, and A. C. Ferrari, Nat. Photon. **4**, 611 (2010).

[9] X. Yu, H. Cheng, M. Zhang, Y. Zhao, L. Qu, and G. Shi, Nat. Rev. Mater. **2**, 17046 (2017).

[10] E. Hobi, Jr., R. B. Pontes, A. Fazzio, and A. J. R. da Silva, Phys. Rev. B **81**, 201406(R) (2010).

[11] T. B. Martins, R. H. Miwa, A. J. R. da Silva, and A. Fazzio, Phys. Rev. Lett. **98**, 196803 (2007).

[12] C. R. Dean, A. F. Young, I. Meric, C. Lee, L. Wang, S. Sorgenfrei, K. Watanabe, T. Taniguchi, P. Kim, and K. L. Shepard, Nat. Nanotech. **5**, 722 (2010).

[13] G. Giovannetti, P. A. Khomyakov, G. Brocks, P. J. Kelly, and J. van den Brink, Phys. Rev. B **76**, 073103 (2007).

[14] G. Le Lay, B. Aufray, C. Leandri, H. Oughaddou, J. P. Biberian, P. de Padova, M. E. Davila, B. Ealet, and A. Kara, Appl. Surf. Sci. **256**, 524 (2009).

[15] B. Aufray, A. Kara, S. Vizzini, H. Oughaddou, C. Leandri, B. Ealet, and G. Le Lay, Appl. Phys. Lett. **96**, 183102 (2010).

[16] J. E. Padilha and R. B. Pontes, J. Phys. Chem. C **119**, 3818 (2015).

[17] E. Bianco, S. Butler, S. Jiang, O. D. Restrepo, W. Windl, and J. E. Goldberger, ACS Nano **7**, 4414 (2013).

[18] J. E. Padilha and R. B. Pontes, Solid State Commun. **225**, 38 (2016).

[19] L. Li, Y. Yu, G. J. Ye, Q. Ge, X. Ou, H. Wu, D. Feng, X. H. Chen, and Y. Zhang, Nat. Nanotech. **9**, 372 (2014).

[20] H. O. H. Churchill and P. Jarillo-Herrero, Nat. Nanotech. **9**, 330 (2014).

[21] J. E. Padilha, A. Fazzio, and A. J. R. da Silva, Phys. Rev. Lett. **114**, 066803 (2015).

[22] J. L. Zhang, S. Zhao, C. Han, Z. Wang, S. Zhong, S. Sun, R. Guo, X. Zhou, C. D. Gu, K. D. Yuan, Z. Li, and W. Chen, Nano Lett. **16**, 4903 (2016).

[23] E. Kan, M. Li, S. Hu, C. Xiao, H. Xiang, and K. Deng, J. Phys. Chem. Lett. **4**, 1120 (2013).

[24] K. Takada, H. Sakurai, E. Takayama-Muromachi, F. Izumi, R. A. Dilanian, and T. Sasaki, Nature (London) **422**, 53 (2003)

[25] S. Walia, S. Balendhran, H. Nili, S. Zhuiykov, G. Rosengarten, Q. H. Wang, M. Bhaskarana, S. Sriram, M. S. Strano, and K. Kalantar-Zadeha, Prog. Mater. Sci. **58**, 1443 (2013).

[26] M. Chhowalla, H. S. Shin, G. Eda, L.-J. Li, K. P. Loh, and H. Zhang, Nat. Chem. **5**, 263 (2013).

[27] Q. H. Wang, K. Kalantar-Zadeh, A. Kis, J. N. Coleman, and M. S. Strano, Nat. Nanotech. **7**, 699 (2012).

[28] W. Choi, N. Choudhary, G. H. Han, J. Park, D. Akinwande, and Y. H. Lee, Mater. Today **20**, 116 (2017).

[29] S. Z. Butler, S. M. Hollen, L. Cao, Y. Cui, J. A. Gupta, H. R. Gutierrez, T. F. Heinz, S. S. Hong, J. Huang, A. F. Ismach, E. Johnston-Halperin, M. Kuno, V. V. Plashnitsa, R. D. Robinson, R. S. Ruoff, S. Salahuddin, J. Shan, L. Shi, M. G. Spencer, M. Terrones, W. Windl, and J. E. Goldberger, ACS Nano **7**, 2898 (2013).

[30] A. H. Castro Neto and K. Novoselov, Mater. Express **1**, 10 (2011).

[31] G. R. Bhimanapati, Z. Lin, V. Meunier, J. Jung, J. Cha, S. Das, D. Xiao, Y. Son, M. S. Strano, V. R. Cooper, L. Liang, S. G. Louie, E. Ringe, W. Zhou, S. S. Kim, R. R. Naik, B. G. Sumpter, H. Terrones, F. Xia, Y. Wang, J. Zhu, D. Akinwande, N. Alem, J. A. Schuller, R. E. Schaak, M. Terrones, and J. A. Robinson, ACS Nano **9**, 11509 (2015).

[32] J. A. Wilson and A. D. Yoffe, Adv. Phys. **18**, 193 (2006).

[33] K. F. Mak and J. Shan, Nat. Photon. **10**, 216 (2016).

[34] X. Xu, W. Yao, D. Xiao, and T. F. Heinz, Nat. Phys. **10**, 343 (2014).

[35] A. Splendiani, L. Sun, Y. Zhang, T. Li, J. Kim, C.-Y. Chim, G. Galli, and F. Wang, Nano Lett. **10**, 1271 (2010).

[36] K. F. Mak, C. Lee, J. Hone, J. Shan, and T. F. Heinz, Phys. Rev. Lett. **105**, 136805 (2010).

[37] G. Wang, X. Marie, I. Gerber, T. Amand, D. Lagarde, L. Bouet, M. Vidal, A. Balocchi, and B. Urbaszek, Phys. Rev. Lett. **114**, 097403 (2015).

[38] A. G. N. Sofiah, M. Samykano, K. Kadirgama, R. V. Mohan, and N. A. C. Laha, Appl. Mater. Today **11**, 320 (2018).

[39] Y. N. Xia, P. D. Yang, Y. G. Sun, Y. Y. Wu, B. Mayers, B. Gates, Y. D. Yin, F. Kim, and H. Q. Yan, Adv. Mater. **15**, 353 (2003).

[40] B. Y. Xia, H. B. Wu, Y. Yan, X. Wen (David) Lou, and X. Wang, J. Am. Chem. Soc. **135**, 9480 (2013).

[41] E. Z. da Silva, A. J. R. da Silva, and A. Fazzio, Phys. Rev. Lett. **87**, 256102 (2001).

[42] F. D. Novaes, A. J. R. da Silva, E. Z. da Silva, and A. Fazzio, Phys. Rev. Lett. **90**, 036101 (2003).

[43] E. Hobi, Jr., A. Fazzio, and A. J. R. da Silva, Phys. Rev. Lett. **100**, 056104 (2008).

[44] R. B. Pontes, E. Z. Silva, A. Fazzio, and A. J. R. Silva, J. Am. Chem. Soc. **130**, 9897 (2008).

[45] H. Liang, M. Upmanyu, and H. Huang, Phys. Rev. B **71**, 241403(R) (2005).

[46] N. Agraït, A. Levy Yeyati, and J. M. van Ruitenbeek, Phys. Rep. **377**, 81 (2003).

[47] J. Wang, Z. Wu, C. Mao, Y. Zhao, J. Yang, and Y. Chen, Sci. Rep. **8**, 4862 (2018).

[48] J. Lin, O. Cretu, W. Zhou, K. Suenaga, D. Prasai, K. I. Bolotin, N. Y. Cuong, M. Otani, S. Okada, A. R. Lupini, J.-C. Idrobo, D. Caudel, A. Burger, N. J. Ghimire, J. Yan, D. G. Mandrus, S. J. Pennycook, and S. T. Pantelides, Nat. Nanotech. **9**, 436 (2014).

[49] X. Liu, T. Xu, X. Wu, Z. Zhang, J. Yu, H. Qiu, J.-H. Hong, C.-H. Jin, J.-X. Li, X.-R. Wang, L.-T. Sun, and W. Guo, Nat. Commun. **4**, 1776 (2013).

[50] A. L. Koh, S. Wang, Can Ataca, J. C. Grossman, R. Sinclair, and J. H. Warner, Nano Lett. **16**, 1210 (2016).

[51] J. C. González, V. Rodrigues, J. Bettini, L. G. C. Rego, A. R. Rocha, P. Z. Coura, S. O. Dantas, F. Sato, D. S. Galvão, and D. Ugarte, Phys. Rev. Lett. **93**, 126103 (2004).

[52] V. Rodrigues, J. Bettini, A. R. Rocha, L. G. C. Rego, and D. Ugarte, Phys. Rev. B **65**, 153402 (2002).

[53] V. Rodrigues, T. Fuhrer, and D. Ugarte, Phys. Rev. Lett. **85**, 4124 (2000).

[54] C. Jin, H. Lan, L. Peng, K. Suenaga, and S. Iijima, Phys. Rev. Lett. **102**, 205501 (2009).

[55] R. Kozubek, M. Tripathi, M. Ghorbani-Asl, S. Kretschmer, L. Madauß, E. Pollmann, M. O'Brien, N. McEvoy, U. Ludacka, T. Susi, G. S. Duesberg, R. A. Wilhelm, A. V. Krasheninnikov, J. Kotakoski, and M. Schleberger, J. Phys. Chem. Lett. **10**, 904 (2019).

[56] S. McDonnell, R. Addou, C. Buie, R. M. Wallace, and C. L. Hinkle, ACS Nano **8**, 2880 (2014).

[57] W. Zhou, X. Zou, S. Najmaei, Z. Liu, Y. Shi, J. Kong, J. Lou, P. M. Ajayan, B. I. Yakobson, and J. C. Idrobo, Nano Lett. **13**, 2615 (2013).

[58] M. Ghorbani-Asl, A. N. Enyashin, A. Kuc, G. Seifert, and T. Heine, Phys. Rev. B **88**, 245440 (2013).

[59] Y.-C. Lin, T. Björkman, H.-P. Komsa, P.-Y. Teng, C.-H. Yeh, F.-S. Huang, K.-H. Lin, J. Jadczak, Y.-S. Huang, P.-W. Chiu, A. V. Krasheninnikov, and K. Suenaga, Nat Commun. **6**, 6736 (2015).

[60] A. W. Robertson, Y.-C. Lin, S. Wang, H. Sawada, C. S. Allen, Q. Chen, S. Lee, G.-D. Lee, J. Lee, S. Han, E. Yoon, A. I. Kirkland, H. Kim, K. Suenaga, and J. H. Warner, ACS Nano **10**, 10227 (2016).

[61] S. Bertolazzi, S. Bonacchi, G. Nan, A. Pershin, D. Beljonne, and P. Samorì, Adv. Mater. **29**, 1606760 (2017).

[62] H.-P. Komsa, J. Kotakoski, S. Kurasch, O. Lehtinen, U. Kaiser, and A. V. Krasheninnikov, Phys. Rev. Lett. **109**, 035503 (2012).

[63] P. Hohenberg and W. Kohn, Phys. Rev. **136**, B864 (1964).

[64] W. Kohn and L. J. Sham, Phys. Rev. **140**, A1133 (1965).

[65] K. Capelle, Braz. J. Phys. **36**, 1318 (2006).

[66] T. Ozaki, Phys. Rev. B **67**, 155108 (2003).

[67] The OpenMX Software Package; http://www.openmx-square.org/ (unpublished).

[68] J. P. Perdew, K. Burke, and M. Ernzerhof, Phys. Rev. Lett. **77**, 3865 (1996).

[69] I. Morrison, D. M. Bylander, and L. Kleinman, Phys. Rev. B **47**, 6728 (1993).

[70] D. Vanderbilt, Phys. Rev. B **41**, 7892 (1990).

[71] T. Ozaki and H. Kino, Phys. Rev. B **69**, 195113 (2004).

[72] G. Theurich and N. A. Hill, Phys. Rev. B **64**, 073106 (2001).

[73] H. J. Monkhorst and J. D. Pack, Phys. Rev. B **13**, 5188 (1976).

[74] I. Horcas, R. Fernandez, J. M. Gomez-Rodriguez, J. Colchero, J. Gomez-Herrero, and A. M. Baro, Rev. Sci. Instrum. **78**, 013705 (2007).

[75] J. Tersoff and D. R. Hamann, Phys. Rev. B **31**, 805 (1985).

[76] A. Togo, F. Oba, and I. Tanaka, Phys. Rev. B **78**, 134106 (2008).

[77] I. Vilfan, Eur. Phys. J. B **51**, 277 (2006).

[78] I. Popov, T. Yang, S. Berber, G. Seifert, and D. Tománek, Phys. Rev. Lett. **99**, 085503 (2007).

[79] W. Wan, B. Xiong, W. Zhang, J. Feng, and E. Wang, J. Phys.: Condens. Matter **24**, 295402 (2012).

[80] T. Thonhauser and G. D. Mahan, Phys. Rev. B **69**, 075213 (2004).

[81] See Supplemental Material at http://link.aps.org/supplemental/10.1103/PhysRevB.100.235416 for (i) orbital-decomposed DOS of the pristine MoS nanowire, (ii) orbital-decomposed DOS of the MoS_2 and (iii) density of states of defective MoS nanowires, (iv) stress (GPa) × strain plot (VASP-DFT plane-wave calculations), and (v) force (nN) × strain plot.

[82] J. E. Padilha, H. Peelaers, A. Janotti, and C. G. Van de Walle, Phys. Rev. B **90**, 205420 (2014).

[83] H.-P. Komsa and A. V. Krasheninnikov, Phys. Rev. B **91**, 125304 (2015).

[84] G. Kresse and J. Furthmüller, Phys. Rev. B **54**, 11169 (1996).

[85] G. Kresse and J. Furthmüller, Comput. Mater. Sci. **6**, 15 (1996).

[86] Chris G. Van de Walle, and J. Neugebauer, J. Appl. Phys. **95**, 3851 (2004).

[87] *CRC Handbook of Chemistry and Physics*, Internet Version, edited by D. R. Lide (CRC Press, Boca Raton, FL, 2005).